4

Lidar and Atmospheric Aerosol Particles

Albert Ansmann and Detlef Müller

Leibniz Institute for Tropospheric Research, Permoserstraße 15, D-04318 Leipzig, Germany (albert@tropos.de, detlef@tropos.de)

4.1 Introduction

Atmospheric aerosols play an important role in many atmospheric processes. Although only a minor constituent of the atmosphere, they have appreciable influence on the Earth's radiation budget, air quality and visibility, clouds, precipitation, and chemical processes in the troposphere and stratosphere. The occurrence, residence time, physical properties, chemical composition, and corresponding complex-refractive-index characteristics of the particles, as well as the resulting climate-relevant optical properties are subject to large diversity especially in the troposphere because of widely different sources and meteorological processes. Therefore, vertically resolved measurements of physical and optical properties of particles such as the particle surface-area concentration, volume and mass concentrations, mean particle size, and the volume extinction coefficient are of great interest. Routine (long-term), height-resolved observations of these parameters can only be carried out with lidar.

Commonly, aerosols are described in terms of aerosol types in climate models. These aerosol types are defined as internal or external mixtures of different components, and each component has distinctive properties. The *water-insoluble* part of aerosol particles consists mostly of soil particles with some amount of organic material. The *water-soluble* part originates from gas-to-particle conversion. It consists of various kinds of sulfates, nitrates, and other water-soluble substances, which also include organics. *Soot* represents absorbing black carbon. *Sea-salt* particles represent the various kinds

of salt contained in seawater. *Mineral* particles describe desert dust produced in arid regions. The *mineral-transported* component describes desert dust that is transported over long distances, which leads to the depletion of large particles. *Sulfate droplets* are used to describe sulfate found in Antarctic aerosol and the stratospheric background aerosol.

Table 4.1 lists some characteristics of important aerosol types used in climate modeling. These aerosol types differ in their relative contribution of the various aerosol components. A detailed overview can be found elsewhere [1, 3]. On the one hand, these types span the average conditions; on the other hand, they take account of extreme conditions for sensitivity studies. It has to be observed that actual measurements may show aerosol properties significantly different from these aerosol types.

The three different types of continental aerosols differ in their amount of soot, which is considered as a parameter describing the influence of anthropogenic activities. Furthermore, the overall concentration of particles strongly increases from continental clean to continental polluted conditions. The urban aerosol describes strong pollution in urban areas. It has the highest concentration of particles, in particular, that

Table 4.1. Properties of aerosol types [1][a]

Aerosol type	N (cm^{-3})	r_{eff} (μm)	*ssa* (0.55 μm)	g (0.55 μm)	$\mathring{a}$ (0.35–0.55 μm)	$\mathring{a}$ (0.55–0.8 μm)
Cont. clean	2600	0.247	0.972	0.709	1.10	1.42
Cont. average	15,300	0.204	0.925	0.703	1.11	1.42
Cont. polluted	50,000	0.150	0.892	0.698	1.13	1.45
Urban	158,000	0.139	0.817	0.689	1.14	0.43
Desert	2300	1.488	0.888	0.729	0.20	0.17
Marit. clean	1520	0.445	0.997	0.772	0.12	0.08
Marit. polluted	9000	0.252	0.975	0.756	0.41	0.35
Marit. tropical	600	0.479	0.998	0.774	0.07	0.04
Arctic	6600	0.120	0.887	0.721	0.85	0.89
Antarctic	43	0.260	1.000	0.784	0.34	0.73
Stratosphere (12–35 km)	3	0.243	1.000	0.784	0.74	1.14

[a]Number concentration is denoted by N. The effective radius r_{eff} describes the mean size of the particle ensemble. The single-scattering albedo *ssa* is defined as the ratio of total scattering to extinction of the investigated particle ensemble. The asymmetry parameter g is a measure of light scattered toward the forward direction compared with the light scattered toward the back direction. The Ångström exponent $\mathring{a}$ [2] describes the spectral slope of the optical coefficients. All numbers hold for a relative humidity of 80%. Effective radius is calculated for 50% relative humidity. A further discussion of some of the parameters is given in Section 4.3.

of soot. Desert aerosol describes the conditions over desert regions without distinguishing between local properties. There are three types of marine aerosols, which contain a different concentration of sea salt depending on the actual wind speed, and soot, which reflects the anthropogenic influence on the maritime environment. Arctic aerosol consists of particles transported from the mid-latitude continental areas and therefore contains soot. The Antarctic aerosol type exhibits a mixture of mostly sulfate droplets with some amount of sea salt and mineral particles. The stratospheric aerosol is given for background conditions.

Elastic-backscatter lidars have extensively been used to investigate clouds and aerosol layers since the early 1960s when Fiocco and Grams [4] reported the first lidar-derived stratospheric aerosol profiles. Only in recent years, however, has significant progress been made toward a quantitative study of atmospheric aerosol properties solely based on lidar. Aerosol lidars were involved in large, integrated aerosol field campaigns such as the Tropospheric Aerosol Radiative Forcing Observational Experiment (J. Geophys. Res. **104**, D2, 1999 and **105**, D8, 2000), the Aerosol Characterization Experiment 2 (Tellus **52B**, No. 2, 2000), the Indian Ocean Experiment (J. Geophys. Res. **106**, D22, 2001 and **107**, D19, 2002), the Lindenberg Aerosol Characterization Experiment (J. Geophys. Res. **107**, D21, 2002), and the Asian Pacific Regional Aerosol Characterization Experiment (J. Geophys. Res. **108**, D23, 2003 and **109**, D19, 2004). These so-called aerosol closure experiments were conducted to study the impact of anthropogenic particles on the climate system. Networks of aerosol lidars such as the Asian Dust Network [5] and the European Aerosol Research Lidar Network [6] were established to investigate the horizontal and vertical distribution of natural and anthropogenic aerosol plumes in a coherent way on a regional to continental scale. The US National Aeronautics & Space Administration (NASA) and, in cooperation, the European Space Agency (ESA) and the National Space Development Agency of Japan (NASDA) will launch satellite-borne lidars for a multiyear mapping of global aerosol distributions and for the characterization of the long-range transport of particles.

In this chapter we review and critically discuss the two most important methods for the determination of optical particle parameters from lidar observations and the techniques that are used to retrieve physical properties of tropospheric and stratospheric aerosols. In Subsection 4.2.1 the technique is explained that is taken to compute the particle backscatter coefficient (scattering coefficient at 180°, normalized to the unit solid

angle) from return signals measured with the widely used elastic or standard backscatter lidar [7–10]. Elastic-backscatter lidars detect the total atmospheric backscatter without separation of particle and molecular contributions to the backscattered signal. The main drawback of this method is that trustworthy profiles of the climate-relevant volume extinction coefficient of the particles cannot be obtained. The extinction profile must be estimated from the determined backscatter-coefficient profile.

By applying the so-called Raman-lidar technique [11, 12] or the high spectral resolution lidar (HSRL) method [13–15] the profile of the particle extinction coefficient can directly be determined. In addition, the profile of the backscatter coefficient is obtained. An aerosol Raman lidar or an HSRL measures two signal profiles, which permit the separation of particle and molecular backscatter contributions. This method is described in Subsection 4.2.2.

For completeness, the scanning or multiangle lidar technique [16–19] is another technique to derive vertical profiles of the particle extinction coefficient. The most critical requirement here is the need for horizontally homogeneous particle backscattering and extinction at all measurement heights. This condition is often not fulfilled, at least not in the convective boundary layer.

Simultaneously measured extinction and backscatter coefficient profiles at several wavelengths between 300 and 1100 nm are the fundamental prerequisite for a successful, accurate retrieval of physical properties of tropospheric particles from the optical ones [20]. Tropospheric aerosols over the continents often contain a complex mixture of natural (marine and dust particles) and anthropogenic particles (mainly sulfate and soot particles) so that the refractive-index characteristics are unknown. Furthermore, because of the great variability of sources and because of coagulation, mixing, transport, and removal processes, the size distribution that covers the particle diameter range from a few nanometers to several micrometers often shows a complex, multimodal shape. The basic methodology of the inversion technique applied to tropospheric lidar observations is explained in Subsection 4.3.1.

Stratospheric aerosol conditions are comparatively simple. As a consequence, much simpler retrieval schemes can be applied here to determine the microphysical properties from lidar data. Sulfuric-acid/water droplets form the stratospheric aerosol layer. For these particles the refractive index is accurately known. The size distribution can well be described by monomodal logarithmic-normal distributions

under background conditions. A second mode is present during several years after major volcanic eruptions. Temporal changes in the size characteristics can be considered to be very slow compared with tropospheric variations. Lidar methods for the retrieval of microphysical properties of stratospheric particles are discussed in Subsection 4.3.2. A few measurement examples illustrating the potential of modern aerosol lidars are presented in Section 4.4.

4.2 Determination of Optical Parameters of Atmospheric Particles

4.2.1 Elastic-Backscatter Lidar

The lidar equation for return signals due to elastical backscatter by air molecules and aerosol particles can, in its simplest form, be written as [7]

$$P(R) = \frac{E_0 \eta_L}{R^2} O(R) \beta(R) \exp\left[-2 \int_0^R \alpha(r)\, \mathrm{d}r\right]. \tag{4.1}$$

$P(R)$ is the signal owing to Rayleigh and particle scattering received from distance R, E_0 is the transmitted laser pulse energy, η_L contains lidar parameters describing the efficiencies of the optical and detection units, and $O(R)$ describes the overlap between the outgoing laser beam and the receiver field of view. $\beta(R)$ (in $\mathrm{km^{-1}\,sr^{-1}}$) and $\alpha(R)$ (in $\mathrm{km^{-1}}$) are the coefficients for backscattering and extinction, respectively. Backscattering and extinction are both caused by particles (index aer) and molecules (index mol):

$$\beta(R) = \beta_{\mathrm{aer}}(R) + \beta_{\mathrm{mol}}(R), \tag{4.2}$$

$$\alpha(R) = \alpha_{\mathrm{aer}}(R) + \alpha_{\mathrm{mol}}(R). \tag{4.3}$$

Molecular absorption effects are ignored. These effects have to be removed from the measured signals before applying the methods presented in this chapter.

Equations (4.1)–(4.3) can be summarized to

$$S(R) = E_0 \eta_L [\beta_{\mathrm{aer}}(R) + \beta_{\mathrm{mol}}(R)] \exp\left[-2 \int_0^R [\alpha_{\mathrm{aer}}(r) + \alpha_{\mathrm{mol}}(r)]\, \mathrm{d}r\right] \tag{4.4}$$

with the range-corrected lidar signal $S(R) = R^2 P(R)$. The overlap is assumed to be complete [$O(R) \equiv 1$], i.e., the minimum distance $R_{\min}$ at which measurements can be made may be defined by $O(R) \leq 1$ for $R \leq R_{\min}$. The molecular scattering properties, $\beta_{\mathrm{mol}}(R)$ and $\alpha_{\mathrm{mol}}(R)$, can be determined from the best available meteorological data of temperature and pressure or approximated from appropriate standard atmospheres so that only the aerosol scattering and absorption properties, $\beta_{\mathrm{aer}}(R)$ and $\alpha_{\mathrm{aer}}(R)$, remain to be determined.

In the next step we introduce the particle extinction-to-backscatter ratio (lidar ratio)

$$L_{\mathrm{aer}}(R) = \frac{\alpha_{\mathrm{aer}}(R)}{\beta_{\mathrm{aer}}(R)} \tag{4.5}$$

in analogy to the molecular lidar ratio

$$L_{\mathrm{mol}} = \frac{\alpha_{\mathrm{mol}}(R)}{\beta_{\mathrm{mol}}(R)} = \frac{8\pi}{3}\ \mathrm{sr}. \tag{4.6}$$

In contrast to the molecular lidar ratio, the particle lidar ratio is range-dependent because it depends on the size distribution, shape, and chemical composition of the particles.

In addition, we introduce the term

$$Y(R) = L_{\mathrm{aer}}(R)[\beta_{\mathrm{aer}}(R) + \beta_{\mathrm{mol}}(R)]. \tag{4.7}$$

In Sasano et al. [10] $Y(R)$ is expressed as a function of $\alpha_{\mathrm{aer}}(R)$.

However, we prefer Eq. (4.7) because the primary information in the measured elastic lidar returns [cf. Eq. (4.1)] is the backscatter coefficient under typical tropospheric conditions with particle vertical optical depth of $\leq$0.3 in the visible spectrum around 550 nm. Under these conditions only the backscatter coefficient can be derived with good accuracy from the elastic backscatter signal.

After substituting $\alpha_{\mathrm{aer}}(R)$ and $\alpha_{\mathrm{mol}}(R)$ in Eq. (4.4) with the expressions (4.5) and (4.6) and inserting $Y(R)$ from Eq. (4.7), the resulting equation can be written as

$$S(R)L_{\mathrm{aer}}(R)\exp\left\{-2\int_0^R [L_{\mathrm{aer}}(r) - L_{\mathrm{mol}}]\,\beta_{\mathrm{mol}}(r)\,\mathrm{d}r\right\}$$
$$= E_0\eta_{\mathrm{L}}Y(R)\exp\left[-2\int_0^R Y(r)\,\mathrm{d}r\right]. \tag{4.8}$$

Taking the logarithms of both sides of Eq. (4.8) and differentiating them with respect to R gives

$$\frac{\mathrm{d}\ln\left(S(R)L_{\mathrm{aer}}(R)\exp\left\{-2\int_0^R [L_{\mathrm{aer}}(r) - L_{\mathrm{mol}}]\,\beta_{\mathrm{mol}}(r)\,\mathrm{d}r\right\}\right)}{\mathrm{d}R}$$
$$= \frac{1}{Y(R)}\frac{\mathrm{d}Y(R)}{\mathrm{d}R} - 2Y(R). \tag{4.9}$$

Finally, we solve Eq. (4.9), known as the Bernoulli equation, for the boundary condition

$$Y(R_0) = L_{\mathrm{aer}}(R_0)[\beta_{\mathrm{aer}}(R_0) + \beta_{\mathrm{mol}}(R_0)] \tag{4.10}$$

to obtain [10]:

$$\beta_{\mathrm{aer}}(R) + \beta_{\mathrm{mol}}(R)$$
$$= \frac{S(R)\exp\left\{-2\int_{R_0}^R [L_{\mathrm{aer}}(r) - L_{\mathrm{mol}}]\,\beta_{\mathrm{mol}}(r)\,\mathrm{d}r\right\}}{\dfrac{S(R_0)}{\beta_{\mathrm{aer}}(R_0) + \beta_{\mathrm{mol}}(R_0)} - 2\displaystyle\int_{R_0}^R L_{\mathrm{aer}}(r)S(r)T(r, R_0)\,\mathrm{d}r}, \quad \text{with}$$
$$T(r, R_0) = \exp\left\{-2\int_{R_0}^r \left[L_{\mathrm{aer}}(r') - L_{\mathrm{mol}}\right]\beta_{\mathrm{mol}}(r')\,\mathrm{d}r'\right\}. \tag{4.11}$$

The profile of the particle extinction coefficient can be estimated from the solution $\beta_{\mathrm{aer}}(R)$ by

$$\alpha_{\mathrm{aer}}(R) = L_{\mathrm{aer}}(R)\beta_{\mathrm{aer}}(R)\,. \tag{4.12}$$

Equation (4.11) can, in principle, be integrated by starting from the reference range R_0, which may be either the near end ($R > R_0$, forward integration) or the remote end ($R < R_0$, backward integration) of the measuring range. Numerical stability, which is not to be mistaken for accuracy, is, however, given only in the backward integration case [8]. This fundamental formalism used to analyze elastic-backscatter lidar data originates from Hitschfeld and Bordan's [21] radar application. However, the technique is often referred to as the Klett method, as Klett [8] introduced the backward integration scheme and restated in this way the Bernoulli solution in a very convenient form for the analysis of lidar observations.

The reference range R_0 in Eq. (4.11) is usually chosen such that at R_0 the particle backscatter coefficient is negligible compared to the

known molecular backscatter value. Such clear-air conditions are normally given in the upper troposphere for laser wavelengths $\leq$700 nm. Note that Rayleigh scattering is proportional to λ^{-4} and thus strongly depends on the wavelength of the transmitted laser pulse.

The most critical input parameter in the Klett method is the particle lidar ratio $L_{\mathrm{aer}}(R)$. As mentioned, this quantity depends on the microphysical, chemical, and morphological properties of the particles. All of these properties, in turn, depend on relative humidity. The lidar ratio can vary strongly with height, especially when marine, anthropogenic (urban, biomass burning), and/or desert dust particles or mixtures of these basic aerosol types are present in layers above each other [22, 23]. Typical lidar ratios of the mentioned different aerosol types as measured with our Raman lidar at 532 nm are given in Table 4.2. Variations between about 20 and 100 sr make it practically impossible to estimate trustworthy extinction profiles from Eq. (4.12). Even in the well-mixed layer, the lidar ratio is not constant with height because relative humidity increases with height. In cases with accompanying sun photometer observations that deliver the optical depth (integral over the extinction coefficient profile), a column-related lidar ratio can be estimated from the ratio of the optical depth to the column-integrated backscatter coefficient determined from Eq. (4.11). This lidar ratio can only be considered as a first guess, the true lidar ratio profile remains unknown.

A long-lasting discussion of achievements and limitations of the lidar method applied may be found in the literature [7–10, 12, 24–29]. The procedure, with all its subsequent modifications and improvements, simply suffers from the fact that two physical quantities, the particle backscatter coefficient and the particle extinction coefficient, must be determined from only one measured quantity, the elastic lidar return.

4.2.2 Raman Lidar and HSRL

This unsatisfactory situation improved significantly when the first Raman lidar experiments demonstrated that accurate vertical profiling

Table 4.2. Typical lidar ratios for different aerosol types at 532 nm wavelength determined with a Raman lidar

Marine particles [22, 30]	20–35 sr
Saharan dust [31]	50–80 sr
Less absorbing urban particles [22, 30]	35–70 sr
Absorbing particles from biomass burning [30, 32]	70–100 sr

of the particle extinction coefficient throughout the entire troposphere is possible [11, 12]. After the Pinatubo eruption in 1991 it was immediately shown that even at stratospheric heights profiles of the volume scattering coefficient can easily be obtained with ground-based Raman lidars [33–36]. First attempts to infer particle extinction properties from Raman signal profiles were reported by Gerry and Leonard [37]. First accurate horizontal transmission measurements with Raman lidar were done by Leonard and Caputo [38].

Two types of lidars for extinction profiling are available. The mentioned Raman lidar measures lidar return signals elastically backscattered by air molecules and particles and inelastically (Raman) backscattered by nitrogen and/or oxygen molecules (cf. Chapter 9).

High spectral resolution lidar (HSRL) (cf. Chapter 5) is the second type of lidar that can be used for the determination of aerosol transmission and light-extinction properties. This lidar relies on the differences in spectral distribution of light elastically backscattered by particles and air molecules. The spectral width of Rayleigh-backscattered photons is increased due to Doppler shifts caused by the thermal motion of the molecules. The thermal motion of aerosol and cloud particles is much slower so their backscatter spectrum remains nearly unchanged. Here, the molecular backscatter channel measures Rayleigh backscattering by blocking the narrow aerosol peak, e.g., by use of an atomic-vapor filter. A second channel may detect the total backscatter or just the central aerosol peak.

Whereas the Rayleigh lidar is operational at day and night, the Raman lidar is mainly used during nighttime, i.e., in the absence of the strong daylight sky background. The strength of Raman signals is a factor of 20 (rotational Raman lines) to 500 (vibration-rotational Raman lines) lower than the one of Rayleigh signals. However, by applying narrow-bandpass filters or a Fabry–Perot interferometer [39] Raman lidar observations are now also possible at daytime with appropriate temporal and spatial resolution [40, 41]. Ground-based solar-blind lidars operating at laser wavelengths well below 300 nm are not appropriate for measurements in the upper troposphere because of strong absorption of laser radiation by ozone.

The determination of the particle extinction coefficient from molecular backscatter signals is rather straightforward. Lidar-ratio assumptions or other critical assumptions are not needed. The advantage of the Raman lidar and the HSRL technique over conventional elastic-backscatter lidar

is already obvious from the respective lidar equation for the molecular backscatter signal,

$$P(R,\lambda_{Ra}) = \frac{E_0 \eta_{\lambda_{Ra}}}{R^2} O(R,\lambda_{Ra}) \beta_{Ra}(R,\lambda_0) \times \exp\left\{-\int_0^R [\alpha(r,\lambda_0)+\alpha(r,\lambda_{Ra})]\,dr\right\}. \quad (4.13)$$

The coefficient β_{Ra} denotes Rayleigh backscattering in the HSRL and Raman backscattering in the Raman case. Particle backscattering does not appear in Eq. (4.13). The only particle-scattering effect on the signal strength is attenuation. $\alpha(R,\lambda_0)$ describes the extinction on the way up to the backscatter region, $\alpha(R,\lambda_{Ra})$ the extinction on the way back to the lidar. For the Rayleigh or the rotational Raman case $\lambda_{Ra} = \lambda_0$ can be used. However, in the case of a vibration-rotational Raman signal the shift of the wavelength from λ_0 before to λ_R after the scattering process must be considered. If, for example, a Nd:YAG laser wavelength of 532 nm is transmitted, the first Stokes vibration-rotation Q branch of nitrogen is centered at $\lambda_{Ra} = 607$ nm.

The molecular backscatter coefficient is calculated from the molecular number density N_{Ra}, which is the nitrogen or oxygen molecule number density for the Raman case and the air–molecule number density for the Rayleigh case, and the molecular (differential) cross section $d\sigma_{Ra}/d\Omega(\pi,\lambda_0)$ for the scattering process (Raman or Rayleigh) at the laser wavelength λ_0 and the scattering angle π:

$$\beta_{Ra}(R,\lambda_0) = N_{Ra}(R)\frac{d\sigma_{Ra}}{d\Omega}(\pi,\lambda_0). \quad (4.14)$$

$\beta_{Ra}(\lambda_0)$ is identical with β_{mol} in Eq. (4.2), if Eq. (4.13) describes a Rayleigh signal. The molecular number density profile is calculated from actual radiosonde observations or standard-atmosphere temperature and pressure profiles.

After inserting the expressions (4.14) into Eq. (4.13), taking the logarithms of both sides of the resulting equations, differentiating them with respect to R, and rearranging, we obtain for the total extinction coefficient

$$\alpha(R,\lambda_0)+\alpha(R,\lambda_{Ra}) = \frac{d}{dR}\ln\frac{N_{Ra}(R)}{S(R,\lambda_{Ra})} + \frac{d}{dR}\ln O(R,\lambda_{Ra}) \quad (4.15)$$

with the range-corrected molecular signals $S(R,\lambda_{Ra}) = R^2 P(R,\lambda_{Ra})$. The overlap term need not be considered for long distances at which

$O(R,\lambda_{Ra}) \equiv 1$. Total laser-beam receiver-field-of-view overlap may in practice not be reached for distances below 2000–3000 m. The measurement range can in these cases be increased (toward the lidar) by correcting for the overlap effect. The correction is based on measurements of the overlap profile with the same lidar under clear sky conditions [42]. However, as can be seen from the relation

$$\frac{d}{dR}\ln O(R,\lambda_{Ra}) = \frac{1}{O(R,\lambda_{Ra})}\frac{d}{dR}O(R,\lambda_{Ra}), \quad (4.16)$$

the determination of the extinction coefficient is rather sensitive to overlap uncertainties close to the lidar where the overlap value is low and changes rapidly with distance.

In the following we concentrate on the optimum measurement range, i.e., we assume proper overlap correction and thus ignore the overlap term in Eq. (4.15). With Eq. (4.3) we can write

$$\alpha_{aer}(R,\lambda_0)+\alpha_{aer}(R,\lambda_{Ra}) = \frac{d}{dR}\ln\frac{N_{Ra}(R)}{S(R,\lambda_{Ra})} - \alpha_{mol}(R,\lambda_0) - \alpha_{mol}(R,\lambda_{Ra}). \quad (4.17)$$

To obtain the extinction coefficient at the transmitted wavelength we have to introduce the Ångström exponent $\mathring{a}(R)$, which describes the wavelength dependence of the particle extinction coefficient,

$$\frac{\alpha_{aer}(\lambda_0)}{\alpha_{aer}(\lambda_{Ra})} = \left(\frac{\lambda_{Ra}}{\lambda_0}\right)^{\mathring{a}(R)}, \quad (4.18)$$

(cf. Table 4.1).

Finally we obtain [11]

$$\alpha_{aer}(R,\lambda_0) = \frac{\frac{d}{dR}\ln\frac{N_{Ra}(R)}{S(R,\lambda_{Ra})} - \alpha_{mol}(R,\lambda_0) - \alpha_{mol}(R,\lambda_{Ra})}{1+\left(\frac{\lambda_0}{\lambda_{Ra}}\right)^{\mathring{a}(R)}}. \quad (4.19)$$

For rotational Raman and HSRL signals the denominator can be set to 2. In contrast to the Klett algorithm, no critical assumption is needed. All the molecular density and scattering terms can be calculated from meteorological or from standard-atmosphere data. Overestimation and underestimation of the $\mathring{a}$ value by 0.5 leads to relative errors of the order of 5%.

As mentioned, in addition to the extinction coefficient, the particle backscatter coefficient can be calculated from the ratio of the aerosol (particle plus Rayleigh) backscatter signal to the molecular backscatter signal as suggested by Cooney et al. [43] and Melfi [44].

The particle backscatter coefficient $\beta_{\text{aer}}(R, \lambda_0)$, now explicitly written as a function of the laser wavelength λ_0, can be determined by using both total (particle + molecular) and pure molecular backscatter signals. Two measured signal pairs $P(R, \lambda_0)$ and $P(R, \lambda_{\text{Ra}})$ at R and R_0 are needed. From two lidar signals $P(R, \lambda_0)$ and $P(R_0, \lambda_0)$ from total backscatter [Eq. (4.1)] and two more lidar signals $P(R, \lambda_{\text{Ra}})$ and $P(R_0, \lambda_{\text{Ra}})$ from molecular backscatter alone [Eq. (4.13)], a solution for the backscatter coefficient $\beta_{\text{aer}}(R, \lambda_0)$ is obtained by forming the ratio [12]

$$\frac{P(R_0, \lambda_{\text{Ra}})P(R, \lambda_0)}{P(R_0, \lambda_0)P(R, \lambda_{\text{Ra}})}, \tag{4.20}$$

inserting the respective lidar equations for the four signals, and rearranging the resulting equation. The solution is

$$\begin{aligned}\beta_{\text{aer}}(R, \lambda_0) + \beta_{\text{mol}}(R, \lambda_0) &= [\beta_{\text{aer}}(R_0, \lambda_0) + \beta_{\text{mol}}(R_0, \lambda_0)]\frac{P(R_0, \lambda_{\text{Ra}})P(R, \lambda_0)}{P(R_0, \lambda_0)P(R, \lambda_{\text{Ra}})}\frac{N_{\text{Ra}}(R)}{N_{\text{Ra}}(R_0)} \\ &\times \frac{\exp\{-\int_{R_0}^{R}[\alpha_{\text{aer}}(r, \lambda_{\text{Ra}}) + \alpha_{\text{mol}}(r, \lambda_{\text{Ra}})]\,\mathrm{d}r\}}{\exp\{-\int_{R_0}^{R}[\alpha_{\text{aer}}(r, \lambda_0) + \alpha_{\text{mol}}(r, \lambda_0)]\,\mathrm{d}r\}}.\end{aligned} \tag{4.21}$$

If the two signal channels are properly aligned so that $O(R, \lambda_{\text{Ra}}) = O(R, \lambda_0)$, then overlap effects cancel out because the backscatter profile is determined from the signal ratio profile $P(R, \lambda_0)/P(R, \lambda_{\text{Ra}})$. As a consequence, the backscatter coefficient can be determined even at ranges very close to the lidar, as will be shown in Section 4.4.

As in the Klett procedure, a reference value for particle backscattering at R_0 must be estimated. To reduce the effect of the uncertainty in this estimate on the solution, it is recommended to choose the reference height in the upper troposphere where particle scattering is typically negligible compared to Rayleigh scattering. Then only the air density, the molecular backscattering, and atmospheric extinction properties must be estimated to solve Eq. (4.21). Again, meteorological profiles or standard-atmosphere data are used to calculate air density and molecular backscatter terms. The particle transmission ratio for the height range

between R_0 and R is estimated from the measured particle extinction profile with the assumption on the wavelength dependence $\lambda^{\dot{a}}$ as used in Eq. (4.19). In the case of the rotational Raman and HSRL signals spectral transmission corrections are not necessary.

Finally, the height profile of the particle lidar ratio,

$$L_{\text{aer}}(R, \lambda_0) = \frac{\alpha_{\text{aer}}(R, \lambda_0)}{\beta_{\text{aer}}(R, \lambda_0)}, \tag{4.22}$$

is obtained from the profiles of $\alpha_{\text{aer}}(R, \lambda_0)$ and $\beta_{\text{aer}}(R, \lambda_0)$ with Eqs. (4.19) and (4.21). For lidars pointed vertically, $R \equiv z$.

4.3 Retrieval of Physical Properties of Atmospheric Particles

Natural particle size distributions can be described rather well by analytic expressions such as logarithmic-normal distributions (e.g., Hinds [45]):

$$\mathrm{d}n(r) = \frac{n_{\text{t}}}{\sqrt{2\pi}\ln\sigma}\exp\left[-\frac{(\ln r - \ln r_{\text{mod,N}})^2}{2(\ln\sigma)^2}\right]\mathrm{d}\ln r. \tag{4.23}$$

$\mathrm{d}n(r)$ denotes the number concentration of particles in the radius interval $[\ln r; \ln r + \mathrm{d}\ln r]$, n_{t} the total number concentration, $r_{\text{mod,N}}$ the mode radius with respect to the number concentration, and σ the mode width, i.e., the geometric standard deviation. Equation (4.23) characterizes a monomodal distribution. Multimodal distributions are sums of ≥ 2 monomodal distributions. The surface-area and volume concentrations follow from Eq. (4.23) by multiplication with $4\pi r^2$ and $4\pi r^3/3$, respectively. Other shapes of particle size distributions are found in, e.g., Hinds [45].

The mean and integral properties of the particle ensemble that are calculated from the inverted particle size distribution are the effective radius, i.e., the surface-area-weighted mean radius

$$r_{\text{eff}} = \frac{\int n(r)\,r^3\,\mathrm{d}r}{\int n(r)\,r^2\,\mathrm{d}r}, \tag{4.24}$$

the total surface-area concentration

$$a_{\text{t}} = 4\pi\int n(r)\,r^2\,\mathrm{d}r, \tag{4.25}$$

and the total volume concentration

$$v_{\text{t}} = \frac{4\pi}{3}\int n(r)\,r^3\,\mathrm{d}r. \tag{4.26}$$

A variety of methods have been proposed since the early 1970s for the retrieval of microphysical particle properties from lidar measurements. These methods can basically be classified into three distinct groups. The first group deals with the combination of a monostatic lidar with some other instrument, e.g., *in situ* instruments carried aboard an aircraft [46] or balloon [47–50]. Applications are restricted to cases such as field campaigns during which such a combination of instruments on an airplane or other airborne platform is most likely to be at hand. It then provides detailed information on microphysical particle properties [51–53]. Extreme care must be taken, however, in the translation of these data into those amenable to comparison with lidar data. Spatial and temporal proximity of the two instruments is very important in the case of observations of the highly variable tropospheric particles. This constraint is less important for stratospheric particles because of the specific conditions prevailing in the stratosphere (cf. Subsection 4.3.2).

A preferred approach is the combined use of lidar with a sun photometer. In that case the treatment of the data from the two instruments is more straightforward. The latter delivers integrated optical depths of the atmospheric column at multiple wavelengths. A mathematical inversion scheme, which is similar to the methods described in Subsection 4.3.1, is used to derive depth-integrated particle size distributions from the sun photometer observations [54]. The combination with lidar observations then allows a rough estimate of the depth-integrated complex refractive index [17]. A few studies deal with the retrieval of particle size and complex refractive index on the basis of bistatic lidar observations [55–57]. Height profiles of this parameter could be derived with supporting data from additional observations with a monostatic lidar and a sun photometer [58]. Comparison with simultaneous *in situ* observations made aboard an aircraft did not show satisfactory agreement.

The drawback in each case is again that two instruments are needed at the same time and in the same location in order to give reliable data on the same particles. In addition, the lidar and sun photometer point in different directions, i.e., away from the sun and into the sun, respectively. For that reason the constraint of observations of the same ensemble of particles cannot be fulfilled in a strict sense, and thus represents an additional source of error.

In the second class of methods Mie-scattering calculations are intended to reconstruct the optical quantities derived from multiwavelength lidar observations [50, 59–62]. For that purpose parameters such as the shape of the particle size distribution and complex refractive

index are assumed *a priori*. Because of the uncertainties associated with such *a priori* assumptions the application of these methods has been restricted to special cases. In the case of stratospheric particles, i.e., polar stratospheric clouds and ejecta from volcanic eruptions, they were quite successful (cf. Subsection 4.3.2). Investigations of noctilucent clouds in the mesosphere have only recently become possible [63–65]. In the case of tropospheric particles only a crude classification into different types of tropospheric particles is possible [59]. In the special case of desert dust results were unsatisfactory [66].

Finally, the third class is a rigorous mathematical approach on the basis of multiwavelength lidar observations. In that respect the technically robust setup of monostatic Raman lidars is almost exclusively considered. The method uses the spectral information contained in the backscatter and extinction information at multiple wavelengths and its change with particle size. First feasibility studies were made by Uthe [67] and by Uthe et al. [68]. Starting from the work of the early 1980s [57, 69] significant progress has been made. Some exploratory work considered the feasibility of multiwavelength observations with a bistatic lidar [70]. But results are not conclusive for a proper assessment of the potential of this technique in view of the difficulties in connection with the experimental setup. A specific technique deals with the retrieval of particle parameters on the basis of multiple-field-of-view observations in the case of multiple-scattering contributions to aerosol lidar returns [71]. This technique is only applicable for particle size parameters >5–10 [72], and so far only considered the case of single-wavelength lidar. The amount of *a priori* information introduced into the mathematical algorithms can be kept lower compared with the methods belonging to class two. The specific use of mathematical tools makes these techniques very versatile and robust with respect to the highly variable properties of tropospheric particles. The basic properties of the successful algorithms used for the retrieval of microphysical particle properties from multiwavelength lidar sounding will be discussed in the following subsection.

4.3.1 Tropospheric Particles

The method of inversion with regularization with constraints [73] is the standard method for the retrieval of microphysical parameters of tropospheric particles from multiwavelength lidar observations [20, 32, 74–78]. Profiles of the physical particle properties follow from the numerical inversion of the vertically and spectrally resolved particle

backscatter and particle extinction coefficients. The optical data are related to the physical quantities through Fredholm integral equations of the first kind:

$$g_i(\lambda_k) = \int_{r_{\min}}^{r_{\max}} K_i(r, m, \lambda_k, s) v(r)\, \mathrm{d}r + \epsilon_i^{\exp}(\lambda_k),$$
$$i = \beta_{\mathrm{aer}}, \alpha_{\mathrm{aer}}, \quad k = 1, \ldots, n. \tag{4.27}$$

The term $g_i(\lambda_k)$ denotes the optical data at wavelengths λ_k in a specific height R. For easier reading, reference to height R will be omitted in the following discussion. The subscript i denotes the kind of information, i.e., whether it is the particle backscatter (β_{aer}) or particle extinction (α_{aer}) coefficient. The data have an error $\epsilon_i^{\exp}(\lambda_k)$. The expression $K_i(r, m, \lambda_k, s)$ describes the kernel efficiencies of backscatter and extinction, respectively. They depend on the radius r of the particles, their complex refractive index m, the wavelength λ_k of the interacting light, as well as the shape s of the particles. For spherical particle geometry the kernel functions $K_i(r, m, \lambda_k, s)$ are calculated from the respective extinction and backscatter efficiencies $Q_i(r, m, \lambda_k)$ for individual particles [79] weighted with their geometrical cross section πr^2:

$$K_i(r, m, \lambda_k) = (3/4r) Q_i(r, m, \lambda_k). \tag{4.28}$$

The term $v(r)$ describes the volume concentration of particles per radius interval $\mathrm{d}r$. The lower integration limit is defined by $r_{\min}$, the radius down to which particles are optically efficient. For measurement wavelengths larger than 355 nm, which is a typical wavelength used for aerosol sounding, the minimum particle size is around 50 nm in radius. The upper limit, $r_{\max}$, is the radius at which concentrations are so low that particles no longer contribute significantly to the signal. For typical particle size distributions in the troposphere $r_{\max}$ is below 10 μm.

In the inversion of Eq. (4.27) the volume concentration is in general preferred over the surface-area or number concentration because it shifts the maximum sensitivity of the kernel efficiencies farther into the optically active range of the investigated particle size distributions. On average this shift leads to a stabilization of the inverse problem (see below). Further improvements of these inversion methods can be expected from a variable use of volume, or surface-area, or number concentration in dependence of the investigated particle size distribution. The main problem which has not been solved yet is how the inversion method by itself can find the most suitable kernel presentation

for each individual data set. First sensitivity studies have been started recently [77, 78].

With the subscript $p = (i, \lambda_k)$ summarizing the kind and number of optical data, Eq. (4.27) is rewritten into the following form:

$$g_p = \int_{r_{\min}}^{r_{\max}} K_p(r, m) v(r)\, \mathrm{d}r + \epsilon_p^{\exp}. \tag{4.29}$$

Equation (4.29) cannot be solved analytically [80, 81]. The numerical solution process [57, 73] leads to the so-called ill-posed inverse problem [82], which is characterized by the incompleteness of the available information, the non-uniqueness of the solutions, and the non-continuous dependence of the solutions on the input data. Even uncertainties as small as round-off errors in the input data lead to unproportionally large changes in the solution.

The retrieval of microphysical particle properties from lidar measurements belongs to the class of severely ill-posed problems [76]. This definition arises from several features connected to lidar observations. Measurement errors are much larger than round-off errors. Incompleteness is given by the small number of measurement wavelengths, as well as the fact that only backscatter and extinction information is available. The non-uniqueness of the solutions follows from the highly complex structure of tropospheric aerosols. They may be multimodal and of variable shape. The complex refractive index of the particles may be wavelength- or size-dependent, or both. Particle shape often deviates from sphericity. Accordingly different combinations of the target parameters may lead to similar optical spectra within the measurement uncertainty.

The first attempt to derive physical quantities on the basis of lidar observations at multiple wavelengths was undertaken with the so-called randomized-minimization-search technique [69]. This approach did not overcome the instability problem in the solution of Eq. (4.29), when an unknown particle size in combination with an unknown complex refractive index was assumed. The more successful technique of inversion with regularization was introduced after that [57, 83–85]. However, the studies still suffered from unrealistic assumptions on the capabilities of aerosol lidar systems, like a large number of measurement wavelengths and/or features such as the number of extinction channels, or the desired particle information was derived under the assumption of a known complex refractive index. The refinement of this method in combination with the development of powerful aerosol lidar systems [31, 86], which make use of Raman channels, resulted in the determination of particle size

parameters and mean complex refractive indices [74] and thus of the single-scattering albedo [87], which is one of the most important parameters in computer models dealing with climate forcing by aerosols. The most significant step in this development was the reduction of measurement wavelengths to a realistic number, currently provided by modern aerosol lidar instruments.

The three inversion algorithms that are used for the routine retrieval of microphysical properties of tropospheric particles [75–77] make use of the techniques described in the following. Base functions are used to select an appropriate subspace from the solution space. Such projection techniques, which originally were introduced by Backus and Gilbert [88, 89], are a necessary condition to turn the ill-posed inverse problem into a well-posed problem [76]. Only the combination of backscatter and extinction coefficients provides for trustworthy particle parameters [20, 77]. A ratio of two to three for the number of backscatter to extinction coefficients can be considered as the optimum choice for the specifications of an aerosol lidar [77], if simplifications for tropospheric particles like wavelength- and size-independence of the complex refractive index are considered. The three standard wavelengths of a Nd:YAG laser, i.e., 355, 532, and 1064 nm, are the minimum number of wavelengths for particle characterization [76, 77, 90], under the above-mentioned simplifications for the complex refractive index. The accuracy increases if backscatter coefficients at up to six wavelengths are used [20, 57, 77].

For the solution of Eq. (4.29) the investigated size distribution $v(r)$ is discretized by a linear combination of base functions $B_j(r)$, also denoted as B-spline functions, and weight factors w_j:

$$v(r) = \sum_j w_j B_j(r) + \epsilon^{\text{math}}(r). \tag{4.30}$$

The right-hand side of Eq. (4.30) contains the mathematical residual error $\epsilon^{\text{math}}(r)$ that is caused by the approximation with base functions. From Eq. (4.30) it is obvious that the inversion codes are not restricted to specific shapes of particle size distributions.

Different shapes of the base functions, denoted as B-splines of order l, are possible. One has to keep in mind that a good reproduction of natural particle size distributions crucially depends on the shape of the base functions. For this reason histogram columns, denoted as B-spline functions of zero degree [69], are not well suited. Triangle functions, known as B-splines of first degree [75, 77, 85], and parabolic functions,

i.e., B-splines of second degree [91, 92], have shown good performance characteristics. In the latter case the shape already implicitly carries detailed structure of naturally occuring particle size distributions and thus can be considered as a rather constraining approach. In the case discussed in Ben-David et al. [91] the set of base functions was augmented by a special class of Junge-type functions [45] in order to account for such special cases of particle size distributions. A new concept makes use of higher-order polynomials [76], which permit a better reconstruction of highly-structured particle size distributions.

The base functions usually are distributed such that their nodes have the same distance on a non-equidistant scale of particle radii, e.g., on a logarithmic radius scale [75, 77, 85]. In that way the base functions make explicit use of the high dynamic range of particle size distributions which extends over several orders of magnitude. On the other hand, narrow size distributions or distributions consisting of particles around the limit of the optically efficient size range may give better results if their nodes are equally distributed on the linear scale of particle radius.

There is no common recipe for the optimum number of base functions. This number may vary with size range, or number of modes, or particularities of the complex refractive index of the investigated size distribution. Some information may be found in Wolfenbarger and Seinfeld [93], Golub et al. [94], Ben-David et al. [91], Müller et al. [75], and Böckmann [76]. The minimum number of base functions is equal to the number of available data points in the algorithms described in Müller et al. [75] and Veselovskii et al. [77]. Eight base functions provide good resolution of monomodal size distributions and give acceptable estimates for bimodal distributions. Improved results are obtained for higher numbers of base function, i.e., approximately 12–14 base functions. A very high number of 68 base functions was used in theoretical studies in Ben-David et al. [91]. In that case 15 measurement wavelengths, very accurate optical data, and a known complex refractive index were assumed, all of which is rather unrealistic in view of lidar instrumentation. Basically the increase of number of base functions can also be achieved by the use of polynomials of higher order [76]. It has to be observed that an increasing number of base functions again results in increasing destabilization of the inverse problem (e.g., Nychka et al. [95]).

In general the exact position of the investigated particle size distribution along the size range used by Eq. (4.29) is not known. The problem is overcome by the use of a so-called inversion window of variable width

and variable position along the investigated size range [75]. Within this inversion window the base functions are arranged next to each other as described before. No sensible solutions are obtained if the inversion window does not cover the position of the investigated particle size distribution. In that respect the shifting inversion window can be regarded as a filter function. Currently 50 different inversion windows within the particle size range from 0.01 to 10 μm are used to obtain an estimate of the position of the particle size distribution [75, 77]. The polynomials of higher order are restricted to a similar size range [76].

The weight factors follow from inserting Eq. (4.30) into Eq. (4.29), and rewriting it into a vector-matrix equation:

$$\mathbf{g} = \mathbf{A}\mathbf{w} + \boldsymbol{\epsilon}. \tag{4.31}$$

The optical data are written as vector $\mathbf{g} = [g_p]$, the weight factors are denoted by $\mathbf{w} = [w_j]$, and the errors are described by $\boldsymbol{\epsilon} = [\epsilon_p]$. $\epsilon_p = \epsilon_p^{\text{exp}} + \epsilon_p^{\text{math}}$ is the sum of experimental and mathematical errors. The matrix $\mathbf{A} = [A_{pj}]$ is called weight matrix [81]. Its elements are given by

$$A_{pj}(m) = \int_{r_{\min}}^{r_{\max}} K_p(r, m) B_j(r)\, \mathrm{d}r. \tag{4.32}$$

The simple solution of Eq. (4.31) for the weight factors,

$$\mathbf{w} = \mathbf{A}^{-1}\mathbf{g} + \boldsymbol{\epsilon}', \tag{4.33}$$

fails to provide reasonable results [81] although the optical data can be reproduced within the error limits $\boldsymbol{\epsilon}$. It is explained by the high dynamic range of several orders of magnitude of the elements of $\mathbf{A}$ and $\mathbf{A}^{-1}$ [20, 81]. Therefore the term $\boldsymbol{\epsilon}' = -\mathbf{A}^{-1}\boldsymbol{\epsilon}$, which describes the respective errors, and $\mathbf{A}^{-1}$, which denotes the inverse of the matrix $\mathbf{A}$, lead to the aforementioned error amplification and discontinuity of the solutions.

Therefore, a procedure is introduced that we call regularization. This technique selects those solutions for which $\boldsymbol{\epsilon}$ in Eq. (4.31) drops below a predetermined minimum value >0. This step is fundamental in the solution process. From first principles it is not possible to exactly reproduce the input optical data from the inversion results. There is always the compromise between the exact reproduction of the optical data and the suppression of error amplification. In the minimization concept, or method of mimimum distance [73, 81], the so-called penalty function e^2 is introduced. It is defined via the simple Euclidian norm $\|\cdot\|$:

$$e^2 \geq \|\mathbf{A}\mathbf{w} - \mathbf{g}\|^2 + \gamma\Gamma(v). \tag{4.34}$$

The penalty function includes physical constraints that are imposed on the solutions and which are determined by the actual underlying physical problem. One differentiates between descriptive and nondescriptive regularization methods [76]. An example for the first method is the use of *a priori* information about the solution itself, e.g., the exact shape of the particle size distribution. A wrong choice of the shape leads in that case to wrong inversion results. Information on the measurement error is another possibility. The algorithm described here employs the non-descriptive regularization method. In this case "smooth" [75, 80, 81] and positive solutions [75, 96, 97] are assumed for the investigated size distribution. The behavior of the particle size distribution in the vicinity of $r_{\min}$ and $r_{\max}$ can also be used as a constraint [75, 77].

The smoothness constraint in Eq. (4.34) is described through the additional penalty term $\Gamma(v)$. $\Gamma(v)$ is a non-negative scalar which measures the deviation of the inverted particle size distribution $v(r)$ from the requested smoothness. With $\mathbf{w}^{\mathrm{T}}$ denoting the transposed of the vector $\mathbf{w}$, the mathematical definition of smoothness $\Gamma(v)$ is given by [81]:

$$\Gamma(v) = \mathbf{w}^{\mathrm{T}}\mathbf{H}\mathbf{w}. \tag{4.35}$$

Smoothing is done in terms of the second derivative of the reconstructed particle size distribution. In the case of eight base functions and eight optical data, this matrix is written as:

$$\mathbf{H} = \begin{bmatrix} 1 & -2 & 1 & 0 & 0 & 0 & 0 & 0 \\ -2 & 5 & -4 & 1 & 0 & 0 & 0 & 0 \\ 1 & -4 & 6 & -4 & 1 & 0 & 0 & 0 \\ 0 & 1 & -4 & 6 & -4 & 1 & 0 & 0 \\ 0 & 0 & 1 & -4 & 6 & -4 & 1 & 0 \\ 0 & 0 & 0 & 1 & -4 & 6 & -4 & 1 \\ 0 & 0 & 0 & 0 & 1 & -4 & 5 & -2 \\ 0 & 0 & 0 & 0 & 0 & 1 & -2 & 1 \end{bmatrix}. \tag{4.36}$$

Other forms of smoothing are presented in Twomey [81], but in general are not used in lidar applications. An innovative approach avoids explicit smoothing through the additional penalty term to allow for better retrieval of multimodal size distributions [76].

The solution of the minimization concept follows from writing inequality (4.34) as an equation, and by expressing $\Gamma(v)$ with Eq. (4.35). With T denoting the respective transposed expressions, the weight vector

w is written as [81]:

$$\mathbf{w} = \left(\mathbf{A}^{\mathrm{T}}\mathbf{A} + \gamma\mathbf{H}\right)^{-1}\mathbf{A}^{\mathrm{T}}\mathbf{g}. \tag{4.37}$$

The inverse problem is stabilized by the matrix $\left(\mathbf{A}^{\mathrm{T}}\mathbf{A} + \gamma\mathbf{H}\right)^{-1}\mathbf{A}^{\mathrm{T}}$.

Figure 4.1 illustrates the concept of regularization. The influence of **H** is determined by the Lagrange multiplier γ. For $\gamma = 0$ there is no smoothing, and only the base functions act as regularization (smoothing) parameter [76]. $\gamma \to \infty$ results in a perfectly smooth solution $v(r)$ which is, however, independent of **g**. As already explained in the context of inequality (4.34), values of $0 < \gamma < \infty$ create solutions for which the oscillating behavior is penalized by $\Gamma(v)$ and thus is suppressed to a certain degree. One chooses as a solution that value of γ for which the complete penalty function in Eq. (4.34) takes a minimum.

The optimum value for the Lagrange multiplier is given by the global minimum of Eq. (4.37), if γ is varied across several orders of magnitude. Different methods can be used to determine this minimum. The exact location of the minimum depends on the respective method, which thus has influence on the quality of the inversion results. A general overview of such methods is found in Engl et al. [98]. With respect to lidar the maximum entropy principle [92], the method of generalized cross-validation [75], the truncated singular value decomposition [76], and the method of minimum discrepancy [77] have been suggested.

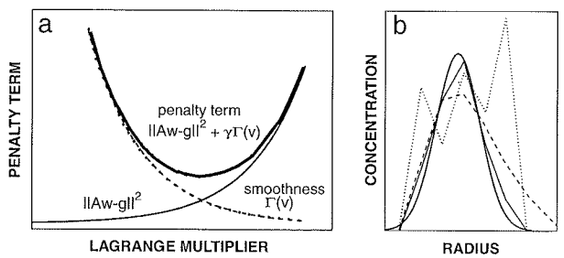

Fig. 4.1. (a) Qualitative illustration of the reconstruction error for increasing smoothing. Shown is the penalty term (thick solid), the error of the reconstructed optical data (thin solid), and the error caused by the smoothing term (dashed). (b) Qualitative effect on the accuracy of the reconstructed particle size distribution. Shown is the case with insufficient smoothing which leads to oscillating solutions (dotted), ideal smoothing, which leads to an ideal reconstruction (thin solid), and the case of strong smoothing which again leads to a false reconstruction (dashed). Also shown is the theoretical particle size distribution (thick solid).

Generalized cross-validation (GCV) has been shown to work quite well [20]. The method explicitly uses the relationship among the input data. It neither needs an *a priori* estimation of the expected error in the data nor an *a priori* assumption of the solution or the statistical and systematic errors. There is only little tendency toward oversmoothing, and low sensitivity to statistical and systematic errors. The closed expression for the calculation of the GCV parameter P_{GCV} is written as

$$P_{\mathrm{GCV}}(\gamma) = \frac{\frac{1}{p}\left\|\left[\mathbf{I} - \mathbf{M}(\gamma)\right]\mathbf{g}\right\|^2}{\left\{\frac{1}{p}\mathrm{trace}\left[\mathbf{I} - \mathbf{M}(\gamma)\right]\right\}^2} \longrightarrow \min. \tag{4.38}$$

I is the unit matrix. The influence matrix

$$\mathbf{M}(\gamma) = \mathbf{A}\left[\mathbf{A}^{\mathrm{T}}\mathbf{A} + \gamma\mathbf{H}\right]^{-1}\mathbf{A}^{\mathrm{T}}, \tag{4.39}$$

is the product of the kernel matrix **A** and the matrix $\left[\mathbf{A}^{\mathrm{T}}\mathbf{A} + \gamma\mathbf{H}\right]^{-1}\mathbf{A}^{\mathrm{T}}$ of Eq. (4.37) [99].

A modified form of the original minimum discrepancy principle also showed good performance [77]. The need for knowing *a priori* the measurement error has been overcome by the use of the modulus $|v(r)|$ of the retrieved particle size distribution. In that case the minimum deviation is calculated from the difference between input optical data and the optical data obtained from $|v(r)|$. The parameter of the modified minimum discrepancy P_{MMD} is calculated as

$$P_{\mathrm{MMD}}(\gamma) = \frac{1}{p}\frac{\|\mathbf{g} - \mathbf{A}|\mathbf{v}|\|}{\mathbf{g}} \longrightarrow \min. \tag{4.40}$$

The global minimum of regularization curves may become rather shallow under certain circumstances [20]. In that case the solutions are not well defined. Averaging of many solutions across the shallow minimum of the discrepancy curve is an elegant new concept [77]. It significantly improves the inversion results and even provides a new approach to error estimation in the inversion.

The discussion given to this point has described the retrieval of the particle volume concentrations for one complex refractive index and for one input optical data set for the (50) different inversion windows. In the case of regularization with GCV this solution space is further constrained. If the measurement errors are known, only those particle volume concentrations are accepted for which the recalculated optical

data are within the uncertainty of the input optical data. In the case of the minimum discrepancy principle the additional constrainment of the solution space implicitly follows from the regularization step.

The solution process described above now has to be carried out for a range of wavelength- and size-independent complex refractive indices, which are given by the kernel functions in Eq. (4.29) [20]. For that purpose one chooses a grid of values for the complex refractive index. The imposed constraints do not allow solutions for some of the complex refractive indices. Consequently, the solution space of this parameter is determined. However, the solution space may be unacceptably large. In such cases the solution space may be further constrained. For example solutions that have optical data closest to the input optical data may serve as constraint. Again it must be observed that the exact reproduction of the input optical data is not possible for theoretical reasons. In addition one can make use of the statistical information within the solution space. If the complex refractive index is correctly chosen, there may be many more inversion windows that provide for sensible particle size distributions compared with complex refractive indices far away from the correct value. However, this property cannot be considered as a general rule. If such solution spaces are visualized in terms of a matrix-like scheme, with x and y representing the real and imaginary axes, one obtains solutions along a diagonal. At some point within this diagonal many more solutions are found than in another region, or the reconstructed optical data, which belong to these solutions, may exhibit a lower deviation to the input optical data compared with the conditions in neighboring areas of the matrix. This area of decreased reconstruction error may serve as a further constrained solution space. Examples for such matrices are found in Müller et al. [87, 90] and Böckmann [76].

Solutions have to be determined for the input data varied within their measurement uncertainty. It is not clear how many variations must be performed until statistically significant results are obtained. This uncertainty is again caused by the numerical solution of the ill-posed problem, which is highly nonlinear, and the actual physical properties that underly the optical data. A discussion can be found in Müller et al. [20] and Böckmann [76]. It is assumed that in general 10–20 different runs provide reliable results.

A severe problem in the inversion is a trustworthy error analysis. Because of the numerical solution process and the highly nonlinear behavior of Eq. (4.29) standard techniques of determining error propagation fail. The methods described above have shown to give acceptable error estimates [32, 77], but cannot be considered as the final solution to

this problem. Future work will also focus on resolving the simplifications that have to be made so far and which present additional sources of uncertainty. Table 4.1 lists the single-scattering albedo which is a wavelength dependent parameter. This wavelength dependence is the result of particle size as well as the fact that particle size distributions may possess a wavelength- and/or size-dependent complex refractive index. The investigation of how accurately parameters of particles of non-spherical geometry can be retrieved will be another challenge. For that purpose particle depolarization measurements at one or several wavelengths will have to be considered in the data retrieval. The most important example of this class of particles is desert dust, see Table 4.1.

4.3.2 Stratospheric Particles

Three different approaches have been applied to describe the long-term trends in the microphysical properties of the stratospheric aerosol layer after the Mount Pinatubo eruption: The conventional, single-wavelength-lidar technique [48, 100, 101], the multiwavelength-backscatter-lidar technique [50, 60–62, 102, 103], and the Raman-lidar technique [36, 49]. Most simple and reliable are the conventional and the Raman lidar technique. These two methods were compared in terms of surface-area and mass concentrations based on dense, 5-year Pinatubo data sets [104].

The conventional and the Raman lidar technique make use of the following relationship between the total surface-area concentration $a_t(z)$ and total volume concentration $v_t(z)$, and the backscatter and extinction coefficients at height z at a single wavelength [49]:

$$\frac{a_t(z)}{\beta_{aer}(z)} = \frac{4}{Q_{\beta,eff}(z)}, \tag{4.41}$$

$$\frac{v_t(z)}{\beta_{aer}(z)} = \frac{4r_{eff}(z)}{3Q_{\beta,eff}(z)}, \tag{4.42}$$

$$\frac{a_t(z)}{\alpha_{aer}(z)} = \frac{4}{Q_{\alpha,eff}(z)}, \tag{4.43}$$

$$\frac{v_t(z)}{\alpha_{aer}(z)} = \frac{4r_{eff}(z)}{3Q_{\alpha,eff}(z)}, \tag{4.44}$$

with the effective scattering efficiencies $Q_{\alpha,eff}(z)$ and $Q_{\beta,eff}(z)$

$$Q_{\alpha,\beta,eff}(m, \lambda, z) = \frac{\int_0^\infty Q_{\alpha,\beta}(r, m, \lambda)n(r, z)r^2\,dr}{\int_0^\infty n(r, z)r^2\,dr}. \tag{4.45}$$

The $Q_{\alpha,\beta}$ [cf. Eq. (4.28)] and, thus, $Q_{\alpha,\beta,\mathrm{eff}}(z)$ depend on the particle size distribution $n(r, z)$ and the refractive index m of the aerosol particles which, in the case of volcanic aerosol, consist of sulfuric acid and water. The sulfuric-acid content of the droplets is mainly a function of temperature and varies between 40% and 85% for temperatures between 195 and 250 K. The refractive index can thus be accurately determined by means of temperature profiles routinely measured with radiosondes. The size distribution $n(z)$ of stratospheric particles is well described by a bimodal logarithmic-normal distribution. Typical median (mode) radii are 0.07–0.1 μm for the stratospheric background mode and 0.3–0.6 μm for the volcanic mode [48].

The surface-area and volume concentrations, $a_t(z)$ and $v_t(z)$, are finally determined by multiplying the backscatter coefficients and/or the extinction coefficients with the respective conversion factors [Eqs. (4.41)–(4.44)]. The mass concentration is obtained by multiplying the volume concentration $v_t(z)$ with the specific gravity of the sulfuric acid droplets. Finally, the effective radius as defined by Eq. (4.24) is simply given by $3v_t/a_t$.

As discussed and illustrated by Jäger and Hofmann [48] and by Jäger and Deshler [101] who performed extensive Mie-scattering calculations and evaluated in this way 20-year measurements of the aerosol size distribution with balloon-borne optical particle counters at Laramie, Wyoming, the conversion factors change considerably with time and height during the first three years after a major volcanic eruption. This change is caused by the change of the particle spectrum, especially by the removal of the second, volcanically induced large particle mode as a result of size-dependent gravitational settling. In that case the effective radius and the scattering efficiencies of the scatterers decrease. It was found that the seasonally averaged conversion factors in the lower stratosphere dropped by a factor of 1.5–3 in the first winter after the El Chichón and the Pinatubo eruptions compared to the respective pre-eruption values. They slowly returned to stratospheric background values during the following three years. Thus, to obtain reliable results from the conventional backscatter-lidar measurements, a time- and height-dependent stratospheric aerosol model is used today that is based on the Laramie measurements. By means of this model, seasonally averaged conversion factors for several stratospheric layers are determined and applied to the lidar data. As a consequence of this procedure, the backscatter-lidar technique is restricted to midlatitudes and cannot be used in the tropics or in polar regions because the temporal and vertical behavior of the aerosol characteristics are unknown there. Furthermore, it is assumed

that the aerosol characteristics found above Laramie at 41° N for a certain height level and time interval are equal to the microphysical properties in the stratosphere over Garmisch-Partenkirchen (47.5° N) in the same height region and for the same time period. Hence, the model-derived conversion factors may be useful in the study of the long-term trend of volcanic effects based on monthly or seasonal mean values of particle parameters, but care must be taken in the interpretation of individual observations of height profiles of the surface-area and volume or mass concentrations.

As shown by Wandinger et al. [49], the conversion factors are functions of the extinction-to-backscatter ratio. The factors can therefore directly be determined with sufficient accuracy from the measured lidar ratio in the case of Raman-lidar observations so that, in the second step, the microphysical properties can directly be determined from the backscatter and extinction profiles. No aerosol model is necessary. This was found from calculations of conversion factors for a large number of measured stratospheric particle size distributions. The Raman-lidar method can therefore be used at very different places on the globe. It was finally shown that the two-wavelength Raman-lidar technique at laser wavelengths of 355 and 532 nm is most promising for stratospheric aerosol profiling. The shorter wavelength is more sensitive to changes in the optical characteristics and in the conversion factors several years after the eruption when the background mode dominates the optical effects. The longer wavelength is optimum during the first two years after the eruption when the volcanic aerosol mode determines the conversion factors. The principal-component analysis of multiwavelength Raman lidar observations as suggested by Donovan and Carswell [35] may be regarded as an alternative approach to the technique suggested by Wandinger et al. [49].

Multiwavelength backscatter lidar is another promising technique for the determination of microphysical parameters. Again, a time- and height-dependent aerosol model is not required. However, this technique suffers from the fact that the key information used in the retrieval procedure is the spectral slope of the backscatter coefficient determined from elastic backscatter signals at two to four different wavelengths. As outlined in Section 4.2, the signal profiles must be calibrated which is crucial for wavelengths ≥ 1 μm. In addition, profiles of the lidar ratio at the laser wavelengths have to be estimated. The assumed lidar ratio profiles sensitively affect the particle backscatter determination at wavelengths ≤ 532 nm. As a consequence, the spectral slope of the backscatter coefficient can only roughly be estimated.

Different approaches to retrieve the physical properties can be found in the literature. The basic idea is the comparison of the spectral slope and strength of the backscatter coefficient obtained from Mie-scattering calculations as a function of number concentration, mode radius, and width of monomodal logarithmic-normal size distributions with the observed backscatter-coefficient spectrum. From the size distribution the parameters can then be calculated that best explain the lidar observations of surface-area, volume, and mass concentrations and the effective radius.

4.4 Measurement Examples

4.4.1 Indo-Asian Haze Over the Tropical Indian Ocean

Figure 4.2 shows a lidar measurement taken during the Indian Ocean Experiment (INDOEX), which was conducted in February and March of 1999 in the tropical Indian Ocean. The observation was made with a scanning 6-wavelength-11-channel aerosol lidar [86] at Hulule Island, Maldives (4° N, 73° E). Two Nd:YAG and two dye lasers served as radiation sources at 355, 400, 532, 710, 800, and 1064 nm. A beam combination unit was used to align all six laser beams onto one optical axis. The combined beam was then directed into the atmosphere at any zenith angle between −90° and +90° by means of a steerable mirror.

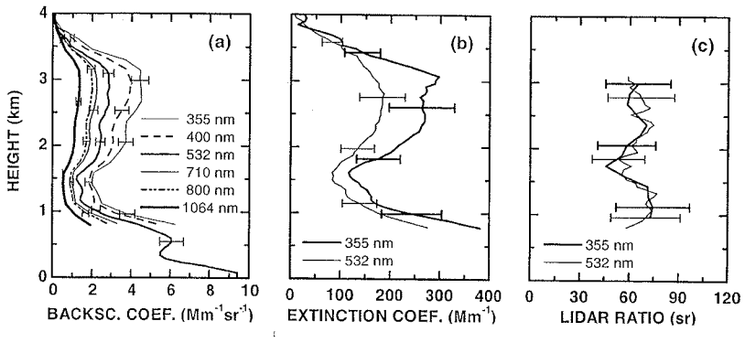

Fig. 4.2. Profiles of (a) backscatter and (b) extinction coefficient, and (c) lidar ratio measured on March 25, 1999 [105]. Error bars denote standard deviations caused by signal noise and systematic errors resulting from the estimates of input parameters. Because of large uncertainties introduced by the overlap effect and detector problems at 355 nm only the 532-nm backscatter profile is trustworthy down to the ground.

The profiles shown in Fig. 4.2 were taken at a zenith angle of 30°. In addition to the return signals elastically backscattered by air molecules and particles at the laser wavelengths, Raman signals from nitrogen molecules were detected at 387 nm (355 nm primary wavelength) and 607 nm (532 nm primary wavelength), and from water-vapor molecules at 660 nm (532 nm primary wavelength). At 710 nm, the cross- and parallel-polarized component (with respect to the plane of polarization of the emitted laser light) of the backscattered signals were detected separately.

The example in Fig. 4.2 shows strongly absorbing anthropogenic pollution advected from the Indian subcontinent to the lidar site [105]. The particle backscatter and extinction coefficients at 355 and 532 nm were determined using the Raman-lidar method (Subsection 4.2.2). The backscatter profiles at 400, 710, 800, and 1064 nm were obtained with the Klett method (Subsection 4.2.1). The lidar ratio profiles were calculated from the backscatter and extinction profiles at 355 and 532 nm. Detector problems at 355 nm and large uncertainties in the overlap correction prohibited the computation of the optical parameters below about 800 m height.

As can be seen in Fig. 4.2, several aerosol layers were present over the Maldives on March 25, 1999. Above the polluted marine boundary layer that reached into heights of 1000 m, a continental Indian pollution plume extended up to 4000 m height. The extinction values were rather large with values of 150–300 Mm^{-1} ($Mm^{-1} = 10^{-6}\,m^{-1}$) in the lofted, free tropospheric aerosol layer. The 532-nm particle optical depth was close to 0.6. The lofted layer contributed more than 60% to the total particle optical depth. The optical depth of the marine boundary layer was 0.2 and a factor of 2–3 larger than values obtained under unperturbed, clean conditions. The lidar ratios were often between 60 and 90 sr during INDOEX [30]. This finding is consistent with the presence of a considerable amount of strongly absorbing particles in South Asian aerosol pollution.

Such an aerosol layering as presented in Fig. 4.2 cannot be resolved with ground-based or spaceborne passive remote sensing. Only active remote sensing allows a detailed, height-resolved analysis of this interesting and, from the point of view of climate and environmental research, very important measurement case.

Figure 4.3 shows the corresponding profiles of the microphysical properties determined with the inversion scheme outlined in Subsection 4.3.1. Mean effective radii are approximately 0.17 μm below 1000 m height. Rather height-independent mean values of 0.14–0.18 μm in

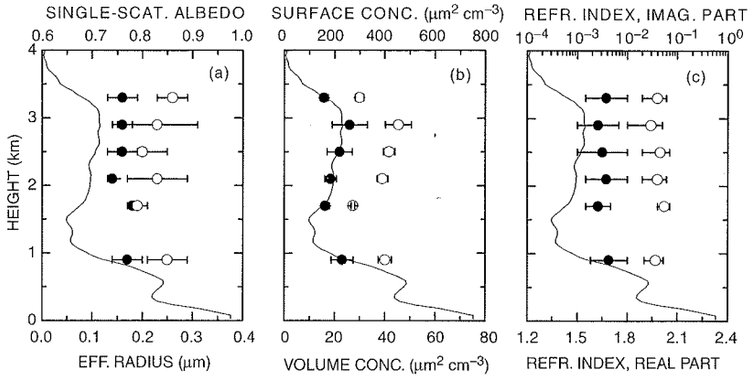

Fig. 4.3. Profiles of (a) effective radius (●) and single-scattering albedo (○), (b) volume concentration (●) and surface-area concentration (○), and (c) mean values of the real (●) and imaginary part (○) of the complex refractive index [106, 107]. The error bars for the particle size parameters indicate the standard deviation. For the inversion the profiles were averaged across layers of 400 m thickness. The solid curve in each of the figures shows the 532-nm particle backscatter coefficient.

the upper layer indicate a well-mixed pollution plume of aged, anthropogenic aerosol particles. The air masses traveled about six days from the highly industrialized and populated northern parts of India. They crossed the Bay of Bengal before they reached the Maldives with the prevailing northeast trade winds. The single-scattering albedo ranged between 0.79 and 0.86. These low values are also representative for strongly absorbing particles which are believed to lead to a warming of the climate, as opposed to sulfate particles which are the main component of North American and European aerosols. The imaginary part shows rather high values between $0.01i$ and $0.08i$ and is much larger than the typical value found for marine aerosols. The real part of the refractive index varies between 1.5 and 1.8, with values centered around 1.65. The mean volume concentration varies between 16 and 26 $\mu m^3/cm^3$. Mean surface-area concentrations vary between 270 and 450 $\mu m^2/cm^3$.

In this example of an Indian pollution plume, the imaginary part of the complex refractive index is an order of magnitude larger than corresponding values found for non-absorbing European pollution observed during the Aerosol Characterization Experiment 2 [108]. The volume concentration is approximately 40% larger, the surface-area concentration is 10–20% larger. Particles from biomass burning observed over Germany after long-range transport from northwest Canada during the Lindenberg

Aerosol Characterization Experiment showed comparably large imaginary parts [32]. However, volume and surface-area concentrations were on average lower by a factor of 2–10.

4.4.2 Mount–Pinatubo Aerosol Layer

Figures 4.4 and 4.5 show two examples of stratospheric aerosol observations over Germany after the Pinatubo eruption which is believed to be the strongest perturbation of the stratospheric aerosol layer in the past century. The Raman lidar measurement in Fig. 4.4 was performed at Geesthacht (GKSS Research Center, 53.4° N, 10.4° E) during the first spring after the eruption when the aerosol loading was highest. Extinction coefficients reached values characteristic for thin cirrus and the surface-area and mass concentrations were a factor of 30–100 above the stratospheric background values. The surface-area concentration was clearly above the threshold value of 15–20 mm^2m^{-3} ($1\,mm^2m^{-3} = 1\,\mu m^2cm^{-3}$) during the first winters after the Pinatubo eruption. At such high values of surface area available for heterogeneous chemical reactions a significant ozone reduction was observed in many places around the globe. The uncertainties in the physical parameters retrieved with the Raman-lidar method (Subsection 4.3.2) are discussed in detail by Wandinger et al. [49]. The error bars in Fig. 4.4 include both statistical and systematic (retrieval) errors. The uncertainties are relatively large because of the ozone absorption correction necessary at the measurement wavelength of 308 nm. The overall uncertainties would decrease by about 30% in the case of a laser wavelength of 355 nm at which absorption by ozone is negligible.

The evolution of the stratospheric aerosol layer in terms of the mass concentration over Geesthacht in northern Germany and Garmisch-Partenkirchen (47.5° N, 11.1° E) in southern Germany is presented in Fig. 4.5. Monthly mean values obtained with the conventional lidar and the Raman-lidar technique are compared. A very good agreement was found in the central and lower part of the volcanic aerosol layer. The perturbation of the stratospheric aerosol layer declined with a 1/e decay time of 13 to 13.5 months in terms of the mass concentration.

The good agreement between the two data sets confirms, on the one hand, the capability of a conventional backscatter lidar, constrained to a realistic aerosol model, to monitor the aerosol parameters most important for climate and ozone–chemistry research. These measurements were carried out to yield monthly or seasonal mean values. The agreement

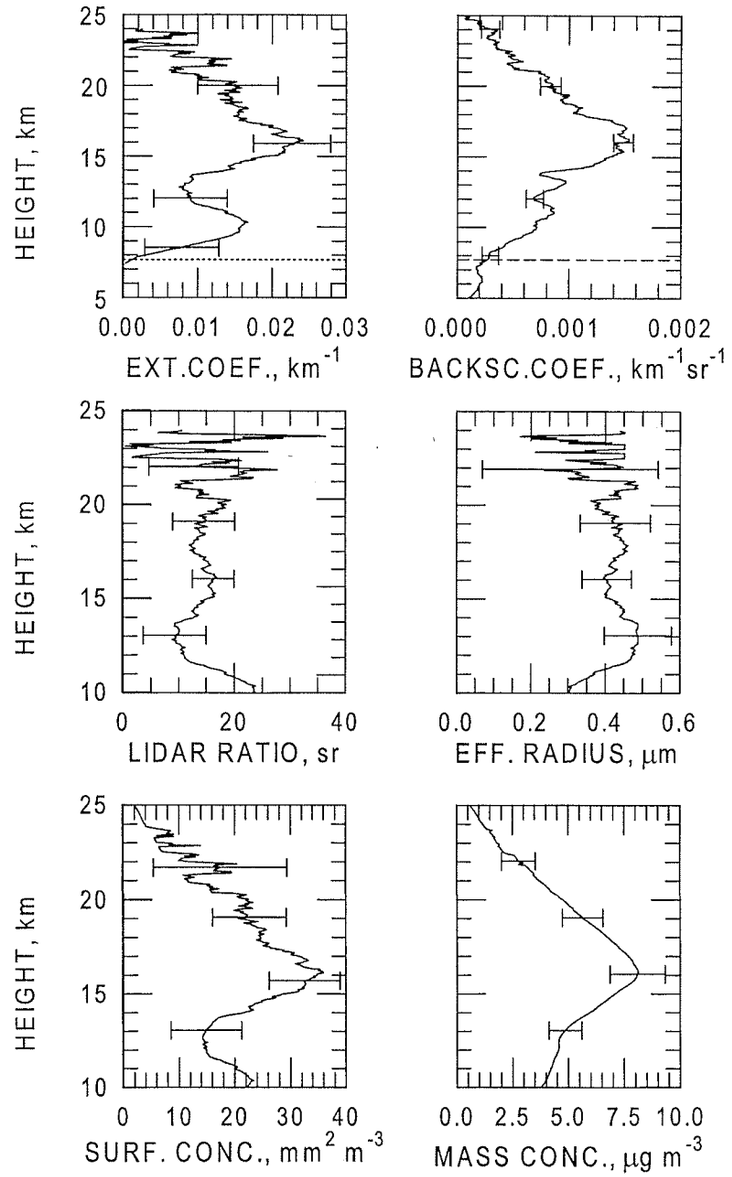

Fig. 4.4. Particle extinction and backscatter coefficients at 308 nm, the extinction-to-backscatter ratio at 308 nm, the effective radius of the particle size distribution, and the particle surface-area and mass concentrations [36]. The measurement was taken on April 4, 1992. The dashed lines indicate the tropopause. The optical depth of the stratospheric aerosol layer was 0.25. Error bars indicate the overall retrieval error.

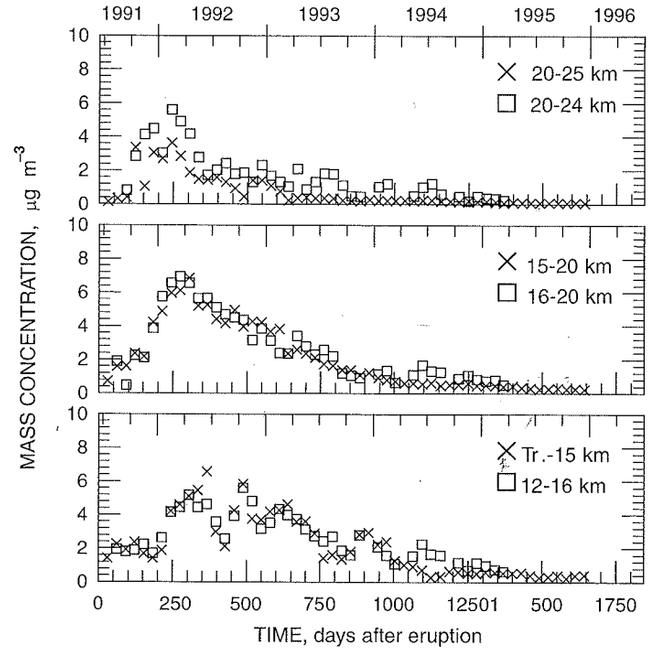

Fig. 4.5. Monthly mean layer–averaged mass concentrations derived from lidar observations at Geesthacht (squares, layers from 12–16 km, 16–20 km, and 20–24 km height) and at Garmisch-Partenkirchen (crosses, layers from the tropopause to 15 km height, 15–20 km, and 20–25 km height) [104]. In terms of the monthly mean mass values integrated from the tropopause to 25 km height, the atmospheric perturbation declined with a 1/e-folding decay time of 13.5 months (Garmisch-Partenkirchen) and 13.3 months (Geesthacht).

corroborates the reliability not only of the Pinatubo–related findings but also of the El-Chichón observations which had already been performed in the way described here. This technique can thus be applied to many single-wavelength lidars monitoring the stratosphere both at northern and southern midlatitudes. On the other hand, the comparison impressively demonstrated the usefulness and, because of its longer list of accessible aerosol parameters, superiority of an aerosol Raman lidar. Because of the attractiveness of this technique, Raman channels are being or have been implemented in many lidars around the world during the past years. It remains to mention that today's aerosol lidar technology enables us to provide the scientific community with vertically resolved information about the relevant aerosol properties needed to

properly describe the impact of aerosols on the Earth's radiation budget and atmospheric chemical processes.

References

[1] M. Hess, P. Koepke, I. Schult: Bull. American Meteorol. Soc. **79**, 831 (1998)
[2] A. Ångström: Tellus **16**, 64 (1964)
[3] G.A. d'Almeida, P. Koepke, E.P. Shettle: *Atmospheric Aerosols: Global Climatology and Radiative Characteristics* (Deepak, Hampton, VA 1991)
[4] G. Fiocco, G. Grams: J. Atmos. Sci. **21**, 323 (1964)
[5] T. Murayama, N. Sugimoto, I. Uno, et al.: J. Geophys. Res. **106**, 18,345 (2001)
[6] J. Bösenberg, A. Ansmann, J.M. Baldosano, et al.: In: *Advances in Laser Remote Sensing. Selected Papers presented at the 20th International Laser Radar Conference (ILRC), Vichy, France, 10–14 July 2000*. A. Dabas, C. Loth, J. Pelon, eds. (École Polytechnique, Palaiseau, France 2001) p. 155
[7] F.G. Fernald, B.M. Herman, J.A. Reagan: J. Appl. Meteorol. **11**, 482 (1972)
[8] J.D. Klett: Appl. Opt. **20**, 211 (1981)
[9] F.G. Fernald: Appl. Opt. **23**, 652 (1984)
[10] Y. Sasano, E.V. Browell, S. Ismail: Appl. Opt. **24**, 3929 (1985)
[11] A. Ansmann, M. Riebesell, C. Weitkamp: Opt. Lett. **15**, 746 (1990)
[12] A. Ansmann, U. Wandinger, M. Riebesell, et al.: Appl. Opt. **31**, 7113 (1992)
[13] S.T. Shipley, D.H. Tracy, E.W. Eloranta, et al.: Appl. Opt. **22**, 3716 (1983)
[14] J.T. Sroga, E.W. Eloranta, S.T. Shipley, et al.: Appl. Opt. **22**, 3725 (1983)
[15] C.J. Grund, E.W. Eloranta: Opt. Eng. **30**, 6 (1991)
[16] P.M. Hamilton: Atmos. Environ. **3**, 221 (1969)
[17] J.D. Spinhirne, J.A. Reagan, B.M. Herman: J. Appl. Meteorol. **19**, 426 (1980)
[18] D. Gutkowicz–Krusin: Appl. Opt. **32**, 3266 (1993)
[19] M. Sicard, P. Chazette, J. Pelon, et al.: Appl. Opt. **41**, 493 (2002)
[20] D. Müller, U. Wandinger, A. Ansmann: Appl. Opt. **38**, 2358 (1999)
[21] W. Hitschfeld, J. Bordan: J. Meteorol. **11**, 58 (1954)
[22] A. Ansmann, F. Wagner, D. Althausen, et al.: J. Geophys. Res. **106**, 20,725 (2001)
[23] A. Ansmann, F. Wagner, D. Müller, et al.: J. Geophys. Res. **107**, 4259, 10.1029/2001JD001109 (2002)
[24] J.D. Klett: Appl. Opt. **24**, 1638 (1985)
[25] L.R. Bissonnette: Appl. Opt. **25**, 2122 (1986)
[26] R. Gonzales: Appl. Opt. **27**, 2741 (1988)
[27] V.A. Kovalev: Appl. Opt. **34**, 3457 (1995)
[28] G.J. Kunz: Appl. Opt. **35**, 3255 (1996)
[29] J. Ackermann: Appl. Opt. **37**, 3164 (1998)
[30] K. Franke, A. Ansmann, D. Müller, et al.: Geophys. Res. Lett. **28**, 4559 (2001)
[31] I. Mattis, A. Ansmann, D. Müller, et al.: Geophys. Res. Lett. **29**, 10.1029/2002GL014721 (2002)

[32] U. Wandinger, D. Müller, C. Böckmann, et al.: J. Geophys. Res. **107**, 10.1029/2000JD00202 (2002)
[33] R.A. Ferrare, S.H. Melfi, D.N. Whiteman, et al.: Geophys. Res. Lett. **19**, 1599 (1992)
[34] M.R. Gross, T.J. McGee, U.N. Singh, et al.: Appl. Opt. **34**, 6915 (1995)
[35] D.P. Donovan, A.I. Carswell: Appl. Opt. **36**, 9406 (1997)
[36] A. Ansmann, I. Mattis, U. Wandinger, et al.: J. Atmos. Sci. **54**, 2630 (1997)
[37] E.T. Gerry, D.A. Leonard: Airport glide slope visual range indicator using laser Raman scattering. *Proccedings*, First International Conference on Laser Applications, Paris, France, 1967
[38] D.A. Leonard, B. Caputo: Opt. Eng. **13**, 10 (1974)
[39] Yu. Arshinov, S. Bobrovnikov: Appl. Opt. **38**, 4635 (1999)
[40] D.D. Turner, R.A. Ferrare, L.A. Brasseur: Geophys. Res. Lett. **28**, 4441 (2001)
[41] D. Müller, I. Mattis, U. Wandinger, et al.: J. Geophys. Res. **108**, 10.1029/2002JD002918 (2003)
[42] U. Wandinger, A. Ansmann: Appl. Opt. **41**, 511 (2002)
[43] J.A. Cooney, J. Orr, C. Tomasetti: Nature **224**, 1098 (1969)
[44] S.H. Melfi: Appl. Opt. **11**, 1605 (1972)
[45] W.C. Hinds: *Aerosol Technology—Properties, Behavior, and Measurement of Airborne Particles* (Wiley, New York 1982)
[46] G.W. Grams, I.H. Blifford, Jr., B.G. Schuster, et al.: J. Atmos. Sci. **29**, 900 (1972)
[47] J.A. Reagan, M.V. Apte, T.V. Bruns, et al.: Aerosol Sci. Tech. **3**, 259 (1984)
[48] H. Jäger, D. Hofmann: Appl. Opt. **30**, 127 (1991)
[49] U. Wandinger, A. Ansmann, J. Reichardt, et al.: Appl. Opt. **34**, 8315 (1995)
[50] M.J. Post, C.J. Grund, A.M. Weickmann, et al.: J. Geophys. Res. **101**, 3929 (1996)
[51] R.A. Ferrare, S.H. Melfi, D.N. Whiteman, et al.: J. Geophys. Res. **103**, 19,673 (1998)
[52] J. Redemann, R.P. Turco, R.F. Pueschel, et al.: J. Geophys. Res. **103**, 23,287 (1998)
[53] J. Redemann, R.P. Turco, K.N. Liou, et al.: J. Geophys. Res. **105**, 9949 (2000)
[54] M.D. King, D.M. Byrne, B.M. Herman, et al.: J. Atmos. Sci. **35**, 2153 (1978)
[55] B.M. Herman, S.R. Browning, J.A. Reagan: J. Atmos. Sci. **28**, 763 (1971)
[56] J.A. Reagan, D.M. Byrne, M.D. King, et al.: J. Geophys. Res. **85**, 1591 (1980)
[57] V.E. Zuev, I.E. Naats, eds.: *Inverse Problems of Lidar Sensing of the Atmosphere* (Springer, Berlin 1983)
[58] J.A. Reagan, J.D. Spinhirne, D.M. Byrne, et al.: J. Appl. Meteorol. **16**, 911 (1977)
[59] Y. Sasano, E.V. Browell: Appl. Opt. **28**, 1670 (1989)
[60] G. Beyerle, R. Neuber, O. Schrems, et al.: Geophys. Res. Lett. **21**, 57 (1994)
[61] M. Del Guasta, M. Morandi, L. Stefanutti, et al.: Appl. Opt. **33**, 5690 (1994)
[62] B. Stein, M. Del Guasta, J. Kolenda, et al.: Geophys. Res. Lett. **21**, 1311 (1994)
[63] G. von Cossart, J. Fiedler, U. von Zahn: Geophys. Res. Lett. **26**, 1513 (1999)
[64] M. Alpers, M. Gerding, J. Höffner, et al.: J. Geophys. Res. **105**, 12,235 (2000)

[65] M. Alpers, M. Gerding, J. Höffner, et al.: J. Geophys. Res. **106**, 7945 (2001)
[66] F. Barnaba, G.P. Gobbi: J. Geophys. Res. **106**, 3005 (2001)
[67] E.E. Uthe: Appl. Opt. **21**, 454 (1982)
[68] E.E. Uthe: Appl. Opt. **21**, 460 (1982)
[69] J. Heintzenberg, H. Müller, H. Quenzel, et al.: Appl. Opt. **20**, 1308 (1981)
[70] H. Yoshiyama, A. Ohi, K. Ohta: Appl. Opt. **35**, 2642 (1996)
[71] L.R. Bissonette: Appl. Opt. **27**, 2478 (1988)
[72] L.R. Bissonette, D.L. Hutt: Appl. Opt. **34**, 6959 (1995)
[73] A.N. Tikhonov, V.Y. Arsenin, eds.: *Solutions of Ill-Posed Problems* (Winston and Sons, Washington, DC 1977)
[74] D. Müller, U. Wandinger, D. Althausen, et al.: Appl. Opt. **37**, 2260 (1998)
[75] D. Müller, U. Wandinger, A. Ansmann: Appl. Opt. **38**, 2346 (1999)
[76] C. Böckmann: Appl. Opt. **40**, 1329 (2001)
[77] I. Veselovskii, A. Kolgotin, V. Griaznov, et al.: Appl. Opt. **41**, 3685 (2002)
[78] I. Veselovskii, A. Kolgotin, V, Griaznov, et al.: Appl. Opt. **43**, 1180 (2004)
[79] C.F. Bohren, D.R. Huffman: *Absorption and Scattering of Light by Small Particles* (Wiley, New York 1983)
[80] D.L. Phillips: J. Assoc. Comput. Mach. **9**, 84 (1962)
[81] S. Twomey, ed.: *Introduction to the Mathematics of Inversion in Remote Sensing and Indirect Measurements* (Elsevier, Amsterdam 1977)
[82] J. Hadamard: Bull. Univ. of Princeton **13**, 49 (1902)
[83] A.P. Ivanov, F.P. Osipenko, A.P. Chaykovskiy, et al.: Izvestiya, Atmos. Oceanic Phys. **22**, 633 (1986)
[84] A. Ben-David, B.M. Herman, J.A. Reagan: Appl. Opt. **27**, 1235 (1988)
[85] P. Qing, H. Nakane, Y. Sasano, et al.: Appl. Opt. **28**, 5259 (1989)
[86] D. Althausen, D. Müller, A. Ansmann, et al.: J. Atmos. Ocean. Tech. **17**, 1469 (2000)
[87] D. Müller, F. Wagner, U. Wandinger, et al.: Appl. Opt. **39**, 1879 (2000)
[88] G. Backus, F. Gilbert: Geophys. J. Roy. Astronom. Soc. **16**, 169 (1968)
[89] G. Backus, F. Gilbert: Philos. Trans. Roy. Soc. London Ser. A **266**, 123 (1970)
[90] D. Müller, U. Wandinger, D. Althausen, et al.: Appl. Opt. **40**, 4863 (2001)
[91] A. Ben-David, B.M. Herman, J.A. Reagan: Appl. Opt. **27**, 1243 (1988)
[92] U. Amato, M.F. Carfora, V. Cuomo, et al.: Appl. Opt. **34**, 5442 (1995)
[93] J.K. Wolfenbarger, J.H. Seinfeld: SIAM J. Sci. Stat. Comput. **12**, 342 (1991)
[94] G.H. Golub, M. Heath, G. Wahba: Technometrics **21**, 215 (1979)
[95] D. Nychka, G. Wahba, S. Goldfarb, et al.: J. Americ. Statist. Association **79**, 832 (1984)
[96] M.D. King: J. Atmos. Sci. **39**, 1356 (1982)
[97] J.K. Wolfenbarger, J.H. Seinfeld: J. Aerosol Sci. **21**, 227 (1990)
[98] H.W. Engl, M. Hanke, A. Neubauer: *Regularization of Inverse Problems* (Kluwer Academic, Dordrecht, The Netherlands 1996)
[99] F. O'Sullivan: Statistical Science **1**, 502 (1994)
[100] H. Jäger, O. Uchino, T. Nagai, et al.: Geophys. Res. Lett. **22**, 607 (1995)
[101] H. Jäger, T. Deshler: Geophys. Res. Lett. **29**, 10.1029/2002GL015609 (2002)
[102] P. Di Girolamo, R.V. Gagliardi, G. Pappalardo, et al.: J. Aerosol Sci. **26**, 989 (1995)

[103] G.S. Kent, G.M. Hansen: Appl. Opt. **37**, 3861 (1998)
[104] A. Ansmann, I. Mattis, H. Jäger, et al.: Contr. Atmos. Phys. **71**, 213 (1998)
[105] A. Ansmann, D. Althausen, U. Wandinger, et al.: Geophys. Res. Letts. **27**, 963 (2000)
[106] D. Müller, F. Wagner, D. Althausen, et al.: Geophys. Res. Lett. **27**, 1403 (2000)
[107] D. Müller, K. Franke, F. Wagner, et al.: J. Geophys. Res. **106**, 28,577 (2001)
[108] D. Müller, A. Ansmann, F. Wagner, et al.: J. Geophys. Res. **107**, 10.1029/2001JD001110 (2002)